On the boundary layer/riblets interaction mechanisms and the prediction of turbulent drag reduction

A. Baron, M. Quadrio and L. Vigevano
Dipartimento di Ingegneria Aerospaziale del Politecnico di Milano, Milano, Italy

Turbulent drag reduction experienced by ribletted surfaces is the result of both (1) the interaction between riblet peaks and the coherent structures that characterize turbulent near-wall flows, and (2) the laminar sublayer flow modifications caused by the riblet shape, which can balance, under appropriate conditions, the drag penalty due to the increased wetted surface. The latter "viscous" mechanism is investigated by means of an analytical model of the laminar sublayer, which removes geometrical restrictions and allows us to take into account "real" shapes of riblet contours, affected by manufacturing inaccuracies, and to compute even for such cases a parameter, called protrusion height, related to the longitudinal mean flow. By considering real geometries, riblet effectiveness is clearly shown to be related to the difference between the longitudinal and the transversal protrusion heights. A simple method for the prediction of the performances of ribletted surfaces is then devised. The predicted and measured drag reduction data, for different riblet geometries and flow characteristics, are in close agreement with each other. The soundness of the physical interpretation underlying this prediction method is consequently confirmed.

Keywords: turbulence; turbulent drag reduction; riblets; conformal mapping

1. Introduction

In the last 15 years several techniques have been developed that aim at reducing the skin friction in turbulent flows. One of the most attractive of these is the use of longitudinal microgrooves, or *riblets* (for a recent review, see Walsh 1990a) cut on the surface of the wall (Figure 1). Ribletted surfaces allow a net turbulent drag reduction of up to 8 percent (Walsh 1982), and possess several features that make them appealing for an industrial application. Their main advantage consists in being a passive drag-reduction technique, namely, one which requires no additional momentum or energy source. Furthermore, the effectiveness of ribletted surfaces is relatively unaffected by misalignment with the direction of the flow (Walsh and Lindemann 1984; Choi et al. 1987) or by compressibility effects (Squire and Savill 1987; McLean et al. 1987), and is virtually insensitive to the presence of longitudinal pressure gradients. Moreover, riblets improve the wall heat transfer (Walsh and Weinstein 1978). Finally, the favorable effect of a ribletted surface adds to those of other drag reduction techniques, such as polymer addition or LEBU devices (Walsh and Lindemann 1984; Coustols et al. 1987). Most of the research carried out on the drag-reducing properties of ribletted surfaces is of experimental nature, and ascertains (e.g., see Walsh 1982; Walsh and Lindemann 1984; Wilkinson et al. 1987; Sawyer and Winter 1987; Wilkinson and Lazos 1987) the geometrical characteristics and the operating conditions necessary to obtain a net turbulent drag reduction. A maximum favorable effect is obtained for a riblet spanwise spacing of about 10–15 wall units. A maximum 8 percent drag reduction is obtained with V-groove riblets of aspect ratio $h/s = 1$. Lower values of the aspect ratio increase the range of values of s^+ where drag reduction is achieved, but it cannot be proved whether they can provide the same maximum drag reduction or not. The shape of the riblet cross section is also of paramount importance, as is the accuracy in manufacturing: it has been proved (Walsh and Lindemann 1984) that a sharp peaky geometry is the most effective. Recent towing tank tests (Walsh 1990b) showed that rounded peaks bring penalties in drag reduction of the order of 40 percent.

Despite the general agreement on the achievable drag reduction, it is still debated how riblets act in modifying the turbulent boundary layer. Two different interpretations, or "interaction mechanisms," have been proposed. The first interpretation (Gallagher and Thomas 1984) explains the drag reduction as coming primarily from a "purely viscous" modification of the sublayer flow, due to the riblet geometry, that promotes the development of low speed regions within the valley of the grooves. This description agrees with the observation that the dimensions of the most effective geometries are of the order of the thickness of the viscous sublayer. It has also been supported

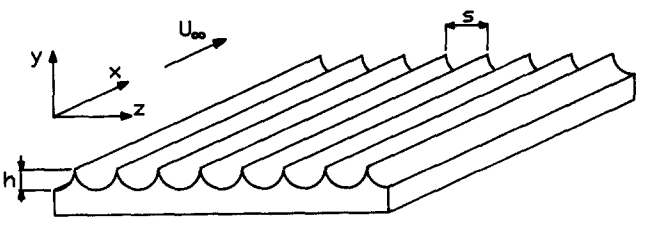

Figure 1 Longitudinal microgrooves, or riblets

Address reprint requests to Professor Baron at Dipartimento di Ingegneria Aerospaziale del Politecnico di Milano, Via C. Golgi 40, 20133 Milano, Italy.

Received 21 April 1992; accepted 16 December 1992

recently by the numerical simulation of laminar flow over a grooved surface carried out by Djenidi et al. (1991), in which a net drag reduction of 2.5 percent was reported, despite the increased wetted area. A different picture is proposed when friction drag in a turbulent boundary layer is supposed to depend primarily on the dynamic process—involving coherent turbulent structures—that has been called the "bursting cycle" (Choi 1989). This second interpretation sees riblet effectiveness as the result of the interaction between the sharp peaks and the spanwise motion of the elongated vortical structures that affect the flow in the buffer layer and in the viscous sublayer.

A theoretical approach aimed at investigating the origin of the riblet effectiveness has been proposed by Bechert and coworkers (Bechert, Hoppe, and Reif 1985; Bechert, Bartenwerfer, Hoppe, and Reif 1986; Bechert and Bartenwerfer 1987, 1989), who, through a simple analytical model of the viscous sublayer, have been able to define a geometrical quantity, named the protrusion height, that expresses the capability of the riblets to affect the boundary layer. Bechert's work implies that the protrusion height characterizes the performances of a ribletted surface, but fails to quantify this in terms of drag reduction. However, using the nondimensional protrusion height for the longitudinal mean flow h_{pl}/s as a correlating parameter, Baron et al. (1989) were able to examine in an unified way the drag-reducing performances of different types of ribletted surfaces and to propose a design criterion for selecting the optimal riblet characteristics. In more recent experimental works by Bechert et al. (1990) and theoretical studies (Luchini et al. 1991), the possibility has been suggested that the key parameter that determines the riblet effectiveness could be the difference between the two protrusion heights for the longitudinal flow and for the cross-flow over the ribletted surface, instead of the simple protrusion height originally defined by Bechert. This hypothesis is also supported by analytical (Landahl 1990) and numerical (Gueznnec et al. 1989) work, which led to an emphasis on the importance of spanwise motions during the bursting cycle and on the damping action of the riblets on such motions.

In the following, the two mechanisms proposed to describe the interaction between riblets and turbulent flow are briefly described. Then Bechert's analysis of the viscous sublayer is extended to deal with arbitrary geometries, which allows us to account for the actual shape of the grooved surfaces. The results of this analysis are eventually utilized in a drag-reduction predictive method, which has been developed based on the two proposed interaction mechanisms.

2. The influence of riblets on the bursting cycle

Extended experimental work carried out at Stanford University (Kline et al. 1967) highlighted the importance of organized deterministic structures in the near-wall turbulence dynamics. This series of events is usually referred to as the *bursting cycle*. Flow visualizations showed that, in the near-wall region of turbulent flows, the viscous layer consists of longitudinally elongated and alternated regions of low- and high-momentum fluid, often called low- and high-speed streaks. These streaks are intermittently lifted away (ejected) from the wall into the buffer region, thus producing highly three-dimensional (3-D) shear-layer structures. The other fundamental type of structure that has been recognized (Blackwelder and Eckelmann 1979) consists of persistent, longitudinal vortices. These represent a secondary flow superposed to the mean spanwise vorticity, and promote a pumping action that enhances momentum diffusion near the wall.

Quantitative information has been obtained from experiments showing that most of the production of Reynolds stresses occurs during the bursting cycle, i.e., during short and intermittent events and, in particular, during the lift-up of the low-momentum fluid. On the other hand, the recent development of computers and methods for the direct numerical simulation of turbulent flows is shedding new light on the understanding of turbulence dynamics. The complexity of multiprobe near-wall measurements makes it in fact prohibitive to carry on exhaustive experiments of this type, while direct numerical simulation allows a complete space-time mapping in three dimensions for all the flow variables of interest. In a recent work by Johansson, Alfredsson, and Kim (1991), a numerical database from an earlier direct numerical simulation of turbulent channel flow was analyzed by means of conditional sampling techniques. Among other interesting results, this study first gave the opportunity of following the space-time evolution of near-wall flow structures, and evidenced strong asymmetries of the instantaneous shear-layer structures. While "in conditional averaging procedures... symmetric patterns are the result of the homogeneity of the flow in the spanwise direction," for instantaneous structures (Figure 2) "the shear is often generated in a process where neighboring elongated high- and low-speed regions interact through a localized spanwise motion." The meandering of high- and low-speed regions thus results in steep streamwise and spanwise velocity gradients.

On the basis of the flow picture depicted above, one can reasonably argue the following: if longitudinal grooves, having dimensions comparable with the thickness of the viscous sublayer, proved to be effective in reducing turbulent friction, they must interact with the spanwise motions taking place in the viscous sublayer itself. To date the details of the interaction are not very clear. It has been supposed (e.g., Bacher and Smith 1985) that the sharp peaks of the riblets reduce the strength of the longitudinal vortices by generating "tertiary" vortices, counterrotating with respect to the secondary ones. The capability of the secondary vortices to induce momentum diffusion, strictly related to their intensity, should be consequently reduced. A different description of the riblet–flow interaction explains the skin-friction reduction through the confining effect of the riblets on the spanwise meandering motions of the low-speed streaks. This possibility has been put forward by Johansson et al. (1991), but has also been suggested by Choi (1989), who observed such motions to be reduced over the ribletted surface, and the average spanwise spacing of the low-speed streaks to be increased, as reported for other drag-reducing techniques such as polymers. In spite of their differences, both the proposed interaction models rely on the effect that the grooved surface has on the cross-flow, somehow associated with the near-wall structures. Both also justify the remarkable dependence of drag reduction on the dimensionless spanwise spacing of the riblets s^+, as revealed by the experiments.

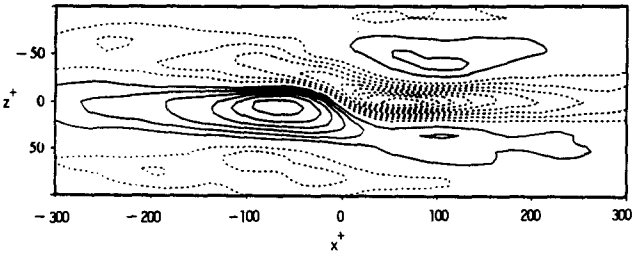

Figure 2 Conditionally sampled u-velocity fluctuations isolines, illustrating typical instantaneous spanwise asymmetric motions (from Johansson et al. 1991)

3. Analysis of the viscous riblet-flow interaction

As mentioned above, the interaction of the riblets with the near-wall coherent structures is an important mechanism in the drag-reduction process. However, it is not the only flow modification that a ribletted surface promotes: a purely viscous interaction acts in fact in the viscous sublayer, which can be even more significant from a quantitative point of view and is capable of counterbalancing the inconvenience of the increased wetted surface.

The linear velocity profile that characterizes the viscous sublayer over a flat plate is modified (Figure 3) by the peak-and-valley shape of the ribletted surface, thus resulting in a change of the wall shear-stress distribution. Shear stresses are increased near the peaks and decreased within the valleys, where the normal velocity gradients are reduced. The modification of the shear-stress distribution results in an average friction coefficient that is lower than the one pertaining to the flat plate. When riblets fully lie in the laminar sublayer, this reduction can compensate for the increased wetted surface.

The effect of this viscous riblet–flow interaction on the mean axial velocity profile has ben analyzed by Bechert and Bartenwerfer (1989) and by Baron et al. (1989) by means of a simplified flow model. By considering riblet heights of the order of the viscous sublayer, the Navier–Stokes equation for the u velocity component in the flow direction, namely,

$$\frac{\partial u}{\partial t} + u\frac{\partial u}{\partial x} + v\frac{\partial u}{\partial y} + w\frac{\partial u}{\partial z} = -\frac{1}{\rho}\frac{\partial p}{\partial x} + \nu\left(\frac{\partial^2 u}{\partial x^2} + \frac{\partial^2 u}{\partial y^2} + \frac{\partial^2 u}{\partial z^2}\right) + f_x \tag{1}$$

can be reduced, in the case of a steady boundary-layer flow of an incompressible fluid over a flat plate, and assuming negligible convective terms, to the Laplace's equation for the u component in the cross-sectional plane y–z:

$$\frac{\partial^2 u}{\partial y^2} + \frac{\partial^2 u}{\partial z^2} = 0 \tag{2}$$

with the boundary condition $u = 0$ at the wall.

Velocity profiles over ribletted surfaces can then be obtained by means of a conformal mapping technique. A neat way to visualize the problem is to consider the flow field over the flat plate as described by an orthogonal, equally spaced mesh, in which lines parallel to the wall correspond to constant values of velocity u, while lines perpendicular to the wall represent constant ΔF lines, where ΔF is the friction force acting on the portion of fluid delimited by two adjacent ΔF lines. These pesudo-stream function lines and pseudo-equipotential lines

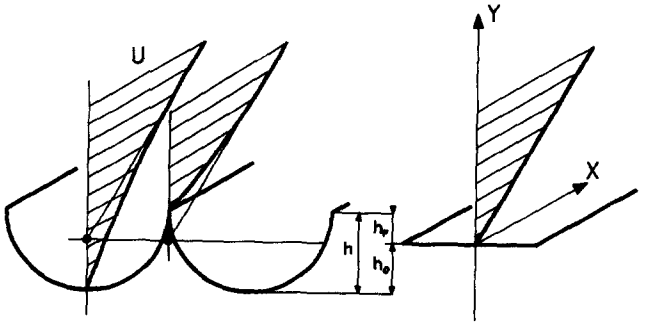

Figure 3 Velocity profile modification over a ribletted surface

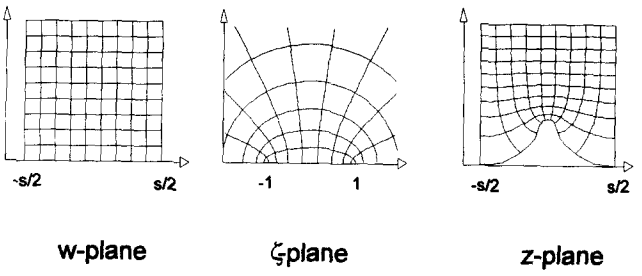

Figure 4 Conformal transformations from the w- to the ζ-plane

are conformally transformed into the mapped plane in which the riblet geometry (Figure 4) is reproduced, thus immediately yielding the solution.

The friction force on the riblet geometry could be obtained from the aforementioned solution by integrating the computed shear stress profile. However, it can be observed that, because of the properties of the solution of the Laplace equation, such calculation is unnecessary. The two pseudo-equipotential lines that define the force acting on the spanwise distance s on the flat plate are in fact mapped into the corresponding periodic locations (peaks or valleys) on the grooved surface of period s, thus yielding the same total friction force over one period. This observation confirms that, when the aforesaid analysis is applicable, the amount of friction drag for the flat and ribletted surfaces is equal, despite the difference in their wetted areas. It is worth mentioning that the results of Djenidi et al. (1991) confirm, at least for a laminar boundary layer, that when the riblet heights are of the order of the linear sublayer thickness, the flow over them is governed by a Laplace's equation. The lines of constant longitudinal velocity computed in Djenidi et al. (1991) practically coincide with the mesh lines obtained through a conformal transformation. The reported 2.5 percent drag reduction in laminar flow could be interpreted as the result of considering the full boundary-layer equations, but could also be affected by the inherent difficulty in determining the friction coefficient distribution and the friction force by numerical integration.

The simplified analysis of the sublayer flow also allows us to assess the influence of the riblets on the sublayer through a geometrical parameter, the protrusion height, first derived by Bechert et al. (1986) in order to define the apparent origin h_0 of the velocity profile on a ribletted surface. The apparent origin is the elevation from the valleys of the ribletted surface at which the boundary layer sees an equivalent smooth wall. It can be thought of as the center of gravity of the shear stress distribution on the ribletted surface (Figure 3). The protrusion height is defined as $h_p = h - h_0$ and quantifies how much riblet peaks protrude into the flow. The apparent origin h_0 can be computed for each riblet shape by comparing the solutions for the flows over the flat plate and over the ribletted surface.

The solutions of Laplace's equation presented by Bechert and Bartenwerfer (1989) and by Baron et al. (1989) were obtained in closed form through a conformal mapping of different riblet shapes of practical interest (e.g., sawtooth, scalloped, and fence types). However, the geometry of the riblets that can be amenable to a closed-form solution is somewhat restricted. For example, solutions for triangular riblets could be derived, from a Schwartz–Christoffel mapping, only for specific values of the apex angle, namely, $\alpha = 2\pi/n$, with n an integer. Still using a conformal mapping technique, the present work removes this restriction, allowing the analysis of virtually any kind of riblet shape, including the irregular shapes that have been reported from the optical measurements of actual riblet contours.

The general form of the Schwartz–Christoffel theorem is

$$\frac{dz}{d\zeta} = f(\zeta) = M \prod_{i=1}^{n} (\zeta - a_i)^{\alpha_i/\pi} \tag{3}$$

which, once integrated, gives

$$z = \int_0^{\zeta} f(\zeta) d\zeta + N \tag{4}$$

This transformation maps the upper half of the ζ-plane into the interior of a polygon or, more generally, into the semiplane bounded by a polygonal line, including n corners, in the z plane. The corner-turning angles α_i are taken positive for counterclockwise rotations, while the complex constants M and N and the real constants a_i have to be determined in order to define the mapping. As mentioned above, this can be accomplished in closed form only for a limited number of special cases. The difficulties in applying the transformation of Equation 3 to arbitrary shapes with any number of corners arise because the relation between a particular wall shape and the numerical values of the parameters of the appropriate transformation is not explicit, thus calling for an iterative procedure.

The constant N is determined by the location of the origin in the transformed plane, and two of the a_i parameters can be chosen arbitrarily. In the present calculations, the values $N = 0$, $a_1 = -1$, and $a_n = 1$ were selected. The remaining parameters of the transformation are calculated using a method of successive approximations, proposed by Davis (1979), as follows. An initial guess is made for M and for the corner locations a_i in the transformed plane, with the constraint that the a_i's are chosen along the real axis of the ζ-plane such that $a_{i-1} < a_i < a_{i+1}$. Integration of Equation 3 is carried out with a modified trapezoidal rule of second-order accuracy. Care has to be taken to avoid large errors near the corners, where the mapping (Equation 3) is not analytic. A composite integration formula that properly accounts for the corner singularities is (Davis 1979)

$$z_{m+1} - z_m = \frac{M}{(\Delta\zeta_m)^{n-1}} \prod_{i=1}^{n} \frac{(\zeta - a_i)^{\alpha_i/\pi + 1}}{\alpha_i/\pi + 1} \Bigg|_{\zeta_m}^{\zeta_{m+1}} \tag{5}$$

where m indicates the generic integration step. As a result of the integration, only the angular rotations at the corners will be found to be correct, while the element lengths of the desired shape in the physical plane will be in error (Figure 5). Then new values of the transformation parameters are determined, such as moving the corners towards their proper locations in the physical plane. The constant M is selected as to bring the last corner (corresponding to a_n) to its correct location, while the new corner locations are obtained by rescaling the a_i parameters as a function of the element length errors as

$$\frac{a_i^{p+1} - a_{i-1}^{p+1}}{a_i^p - a_{i-1}^p} = C \frac{|z_i^{ex} - z_{i-1}^{ex}|}{|z_i^p - z_{i-1}^p|} \tag{6}$$

where p stands for the iteration level, the suffix ex indicates the desired corner position, and the constant C is determined such that $a_n = 1$. This procedure is repeated until the correct location of all the corners is achieved, within a small tolerance. The method has a fast convergence, independent of the selected initial guess.

An extension of the above-mentioned method that is capable of dealing with periodic walls of arbitrary shapes (as in the case of a ribletted surface) has been proposed by Floryan (1986). However, a different approach is used here, and periodicity is accomplished through an additional conformal transformation, which maps the whole ζ-plane into a slab in the w-plane (Figure 4) as

$$\zeta = \sin w$$

Applying then the Schwartz–Christoffel mapping (Equation 3) to a semi-infinite slab in the physical z-plane, one gets the desired correspondence between the plane and the ribletted walls for a periodic configuration.

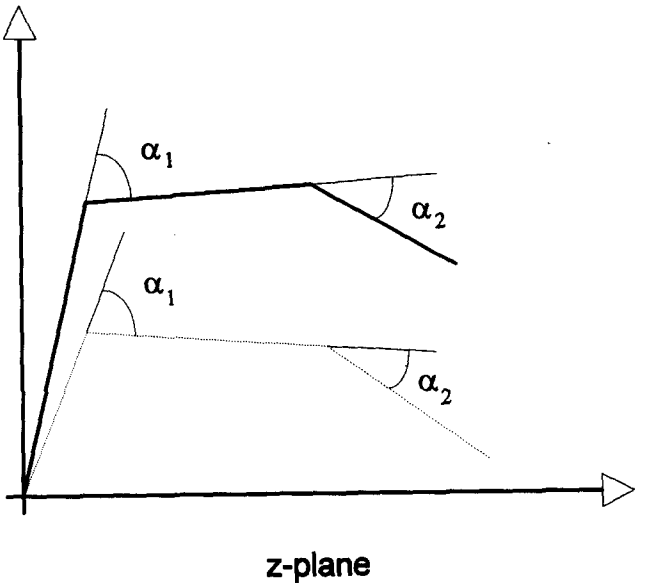

Figure 5 Iterative procedure for the Schwarz–Christoffel transformation of a flat plate into a ribletted wall of arbitrary shape

The above-described conformal mapping technique, capable of handling virtually any shape of riblet contour delimited by a polygonal line, will be used below for computing the longitudinal protrusion height, h_{pL}, for the actual geometry of different types of riblets in order to assess the drag-reduction prediction method presented in the next section.

4. A prediction method

On the basis of the phenomenological and theoretical analyses of the riblet–flow interaction, it is possible to devise a simple prediction method that is capable of assessing the drag-reducing performances of a given ribletted surface. The aim is primarily to confirm the soundness of the physical interpretation of the proposed interaction mechanisms, rather than to provide an accurate quantitative prediction. However, such predictive capability, although approximate, can be used as a guideline to select the more promising shapes among the many possible riblet geometries.

The method makes use of experimental information provided by direct friction-force measurements. As already pointed out, the drag-reduction effectiveness strongly depends on the actual geometry of the grooved surface. It will be shown in section 4.1 that the possibility of analyzing the "true" riblet geometry, as derived from microphotographs, is a key point for correlating the force measurements. For these reasons the database has been assembled by considering only experiments for which both drag measurements and actual riblet geometries are well documented. Therefore a set of experiments by Walsh and Lindemann (1984) has been selected. This results in a somewhat limited but rather accurate database. The data of these authors are particularly reliable, being the result of a continuous refinement of the experimental procedures accomplished during a number of years.

The main assumption of the method is that the variation of turbulent friction drag due to the riblets, with respect to that of a smooth surface, D_r/D_f, is only produced by two mechanisms:

(1) the interaction between riblet peaks and the instantaneous spanwise motions, which can be expressed as a function $\mathbb{F}(s^+)$ of the nondimensional spanwise spacing s^+; and
(2) the viscous sublayer flow modification, given by the function $\mathbb{G}(h_p^+)$, where the nondimensional protrusion height h_p^+ quantifies how much the riblets lie within the sublayer.

Accordingly, the riblet performance can be estimated, in terms of D_r/D_f, as

$$D_r/D_f = \mathbb{F}(s^+) \cdot \mathbb{G}(h_p^+)$$

The modeling function $\mathbb{F}(s^+)$ expresses the amount of drag reduction due to the interaction between riblets and the near-wall structures, and has the following form:

$$\mathbb{F}(s^+) = \begin{cases} \dfrac{\Delta D_{max}}{15^2} s^{+2} - 2\dfrac{\Delta D_{max}}{15} s^+ + 1 & s^+ < 15 \\ (1 - \Delta D_{max}) + \Delta D_{max}(1 - \exp((15 - s^+)/20)) & s^+ > 15 \end{cases}$$

The choice of s^+ as the independent variable is suggested by the experiments, while it is reasonable to suppose that $\mathbb{F}(0) = 1$, assuming the ribletted surface is flat in the limit $s^+ \to 0$. The selected experimental database also shows that the maximum drag reduction takes place around $s^+ = 15$. Fixing the s^+ value for which the maximum drag reduction occurs is certainly a limitation of the present method, since some experimental evidence, especially for blade-type riblets (Wilkinson and Lazos 1987), suggests that such a value somewhat depends on the riblet aspect ratio h/s. This choice, however, allows us to reduce the number of the free parameters of the method. A wider database could also suggest a different optimum s^+ value, i.e., $s^+ = 12$; however, the result of some parametric computations showed no appreciable difference when using $s^+ = 12$ instead of $s^+ = 15$. The procedure followed for determining, at $s^+ = 15$, the maximum drag benefit ΔD_{max} achievable with a particular geometry, will be described in section 4.1.

For $s^+ < 15$, the experimental information is insufficient to suggest a precise functional dependence on s^+. A quadratic dependence of the function $\mathbb{F}$ on s^+ is assumed, with the slope of the curve being zero in correspondence to the minimum at $s^+ = 15$; however, a simple linear relationship could have been equally well assumed. On the other side, an exponential recovery of the drag reduction up to the limit $\mathbb{F} = 1$ (no drag reduction) is used for $s^+ > 15$. The time constant involved in the exponential function has been selected equal to 20, by carefully examining those data sets (for example, Figure 8b and 8c) where $\mathbb{G}(h_p^+) \equiv 1$. A physical meaning for the value of this constant can be argued as follows: in correspondence with the mean spacing of the low-velocity streaks ($s^+ = 100$ as reported by many experiments), the value of the function $\mathbb{F}$ is 0.99, and one can reasonably expect that for this spanwise spacing of the ribs, the interaction with the structures of the flow is almost negligible.

The function $\mathbb{G}(h_p^+)$ is determined as follows. From the simplified theoretical analysis of the viscous interaction, it can be concluded that, when the riblets lie fully within the sublayer, the reduction of the average friction coefficient experienced by the ribletted surface exactly compensates for the increase of the wetted area. This is expressed assuming $\mathbb{G} = 1$ for $h_p^+ < h_{vs}^+$, where h_{vs}^+ is the height of the laminar sublayer, assumed equal to three wall units. On the other extreme, we can suppose that for high values of h_p^+ the riblets are almost completely outside of the sublayer, and experience an increase of drag proportional to the increase of wetted area. This permits us to define the function $\mathbb{G}$, in the limit of $h_p^+ \to \infty$, as $\mathbb{G} = S_r/S_f$, where S_r and S_f are the wetted areas of the ribletted and the smooth surfaces, respectively. The functional form for $\mathbb{G}$ is simply given, as shown in Figure 6, by

$$\mathbb{G}(h_p^+) = \begin{cases} 1 & h_p^+ < h_{vs}^+ \\ R_s + (1 - R_s)\exp[-(h_p^+ - 3)/24] & h_p^+ > h_{vs}^+ \end{cases}$$

where $R_s = S_r/S_f$ and the time constant has been selected in order to reach 90 percent of the maximum drag increase when riblets protrude outside of the buffer layer (i.e., at 40 wall units). It can be observed that, when $h_p^+ > h_{vs}^+$, it becomes incorrect to compute the h_p/s value by the theoretical approach described in section 3, since the Couette-flow analysis is no longer strictly applicable. This does not mean that the assumed $\mathbb{G}$ function is not valid; rather, it is the h_p/s value that should be computed by a more sophisticated analysis. Since this would require the solution of the full Navier–Stokes equations, which is beyond the scope of the present work, it has been assumed that the h_p/s value, computed with the conformal mapping technique of section 3, can be "extrapolated" and used also when $h_p^+ > h_{vs}^+$. This assumption has been justified a posteriori by noting that the computed h_p^+ values, in the range of the considered experimental conditions, never exceed the value of $h_p^+ = 10$, i.e., they lie well inside the buffer layer.

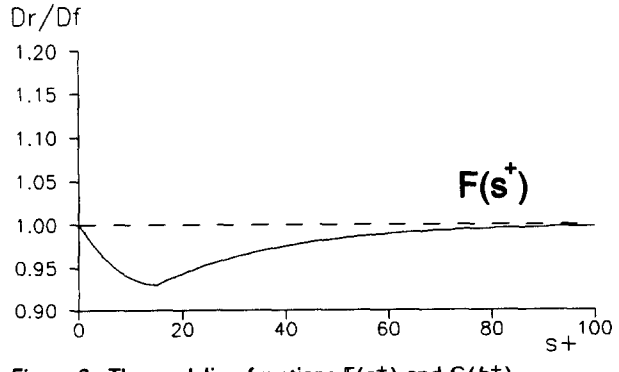

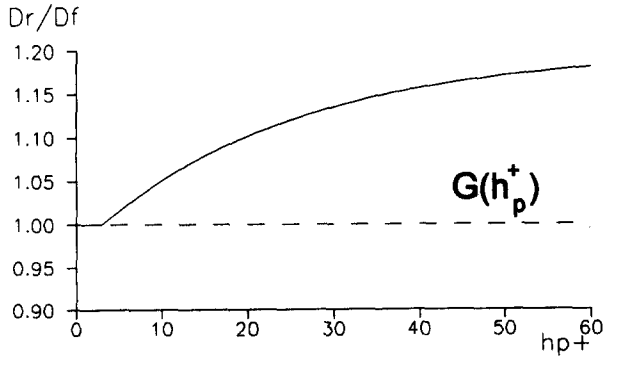

Figure 6 The modeling functions $\mathbb{F}(s^+)$ and $\mathbb{G}(h_p^+)$

4.1 Riblet effectiveness and protrusion heights

In previous works by Bechert and Bartenwerfer (1989) the longitudinal protrusion height h_{pL} has been proved to be somewhat related to the maximum amount of drag reduction, $\Delta D_{max} = ((D_r - D_f)/D_f)_{max}$, associated with a particular riblet geometry. However, it failed to quantify exactly the maximum achievable benefit. A different parameter was recently suggested by Bechert et al. (1990) and Luchini et al. (1991), namely, the difference, $\Delta h_p/s$, between the dimensionless protrusion heights for the longitudinal flow, h_{pL}/s, and for the cross-flow, h_{pC}/s. This parameter is here considered for the prediction of ΔD_{max}.

The cross-flow protrusion height h_{pC}/s is defined in the same way as h_{pL}/s, but referring to the biharmonic instantaneous cross-flow within the laminar sublayer. Values of h_{pC}/s for different ideal riblet geometries have been derived from the results of the boundary-element calculations of Luchini et al. (1991).

In Figure 7a, the values of the maximum amount of drag reduction ΔD_{max} are plotted versus the difference $\Delta h_p/s$. These are computed on the basis of the "ideal" geometry. In spite of its soundness, the assumed hypothesis seems to be contradicted by the poor correlation evidenced in the figure. However, a quite different picture emerges (see Figure 7b) when the "real" geometry of the ribs, as inferred from available microphotographs, is considered instead of the "ideal" one. Here h_{pL}/s is computed using the numerical procedure described in section 3, while h_{pC}/s is still derived from the analytical solution obtained by Luchini et al. (1991), but using the actual dimensions of the ribs instead of the nominal ones. This procedure could obviously be improved by considering the actual geometry also for the calculation of h_{pC}/s. The cross-flow protrusion height h_{pC}/s, however, is much less sensitive than the longitudinal one to possible geometrical imperfections present in actual ribs. For this reason, information contained in Figure 7b can be only negligibly affected by refinements in the evaluation of h_{pC}/s. Note how, in spite of some spreading of the data, associated with the above-mentioned uncertainty in the evaluation of h_{pC} and with additional practical difficulties encountered in inferring riblet geometries from small (and sometimes not so clear) photographs, a linear trend is clearly evident. Moreover, the straight line obtained by a least-squares fit of the performances of different ribs practically passes (as it should) through the origin of the $(\Delta D_{max}) - (\Delta h_p/s)$ plane. This linear correlation between ΔD_{max} and $\Delta h_p/s$ is one of the most important findings of this work. To the best of our knowledge, it constitutes the first experimental support of the hypothesis of Bechert and Luchini, confirming that riblet effectiveness is strictly related to some damping of the instantaneous cross-flow in the near-wall region of a turbulent boundary layer. On the basis of this analysis, the maximum drag reduction expressed by the modeling function $F(s^+)$ is set up by least-squares fitting to the data shown in Figure 7b.

4.2. Validation of the drag-reduction prediction method

The above-described drag-reduction prediction method has been validated by comparing the predicted performances of a variety of geometrical configurations with drag-reduction measurements obtained by various authors. The reliability of the prediction method is best highlighted by its capability in predicting (1) the maximum value of the drag reduction ΔD_{max}, (2) the zero drag-reduction crossover point, and (3) the trend of drag recovery at the higher values of s^+.

In Figure 8 the results of the comparison with the data of Walsh and Lindemann (1984) are presented. Predictions and experimental data, covering a variety of combinations of riblet geometries and flow conditions, are in close agreement. Rare discrepancies, when present (e.g., Figure 8f; model 29 from Walsh and Lindemann 1984), always concern riblet configurations for which the contour of the actual geometry has been inferred from particularly poor-quality photographs. Two further data sets by Sawyer and Winter (1987) and Wilkinson and Lazos (1987) have been used to validate the present method. Sawyer and Winter's set of measurements refers to triangular as well as scalloped riblet shapes, and has been selected because the actual riblet geometry is documented. The result of the comparison between computed and measured drag reduction (Figure 9) shows, for the tested h/s range of 0.4–0.8, a fairly good agreement. The comparison with the experiments of Wilkinson and Lazos (1987) is reported in Figure 10. These measurements have been selected because they deal with a different kind of riblet, namely, a fence- or blade- or L-type shape. Unfortunately, the actual riblet geometry is not documented in this case, so the comparison has been carried out by referring to the nominal geometry and including the quoted blade thickness. The plots in Figure 10 show that, even in this case, a reasonable agreement has been obtained for all but one of the experiments considered.

In general, it can be concluded that the substantial information is well predicted for all the experiments, despite the extreme simplicity of the method.

5. Conclusions

In the present work, it is suggested that riblets reduce turbulent skin friction through two basic mechanisms. The first is a purely

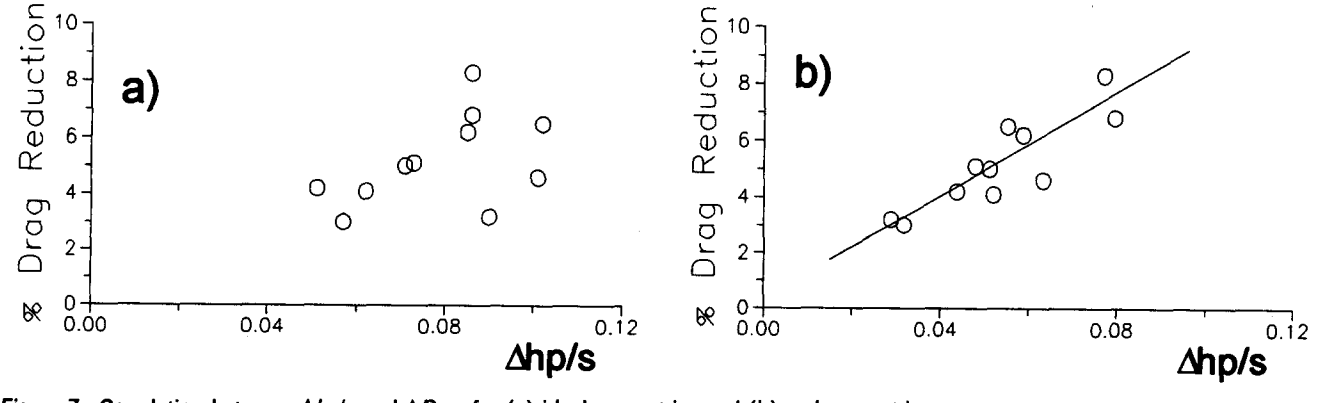

Figure 7 Correlation between $\Delta h_p/s$ and ΔD_{max} for (a) ideal geometries and (b) real geometries

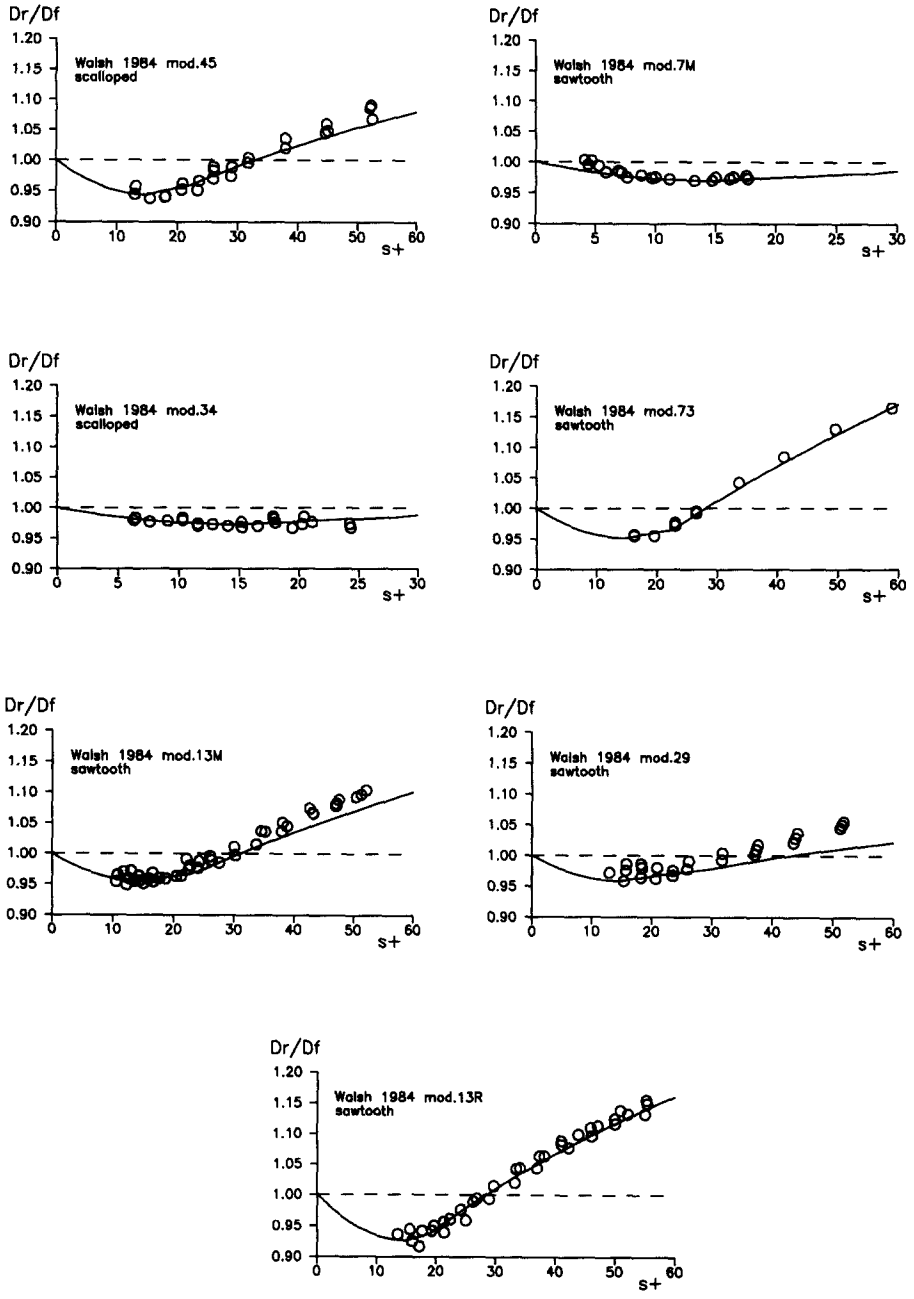

Figure 8 Comparison between measured (symbols) and predicted (solid lines) drag data for various ribletted surfaces. Experimental data from Walsh and Lindemann (1984)

viscous interaction, which allows us to completely compensate for the drag penalties associated with an increased wetted area, provided the ribletted surfaces behave as "aerodynamically smooth" surfaces (i.e., when riblets completely lie within the laminar sublayer). The second concerns the influence of the riblets on the near-wall turbulent structures, and implies some damping action on the instantaneous cross-flow in the turbulent boundary layer.

The former mechanism is analyzed by means of a numerical method that allows the calculation of a parameter, namely, the longitudinal protrusion height h_{pL}, for riblets of arbitrary shape. This numerical method allows us to treat "real" instead of "ideal" riblet geometries, namely, to take into account possible manufacturing inaccuracies. This capability proves to be essential in confirming the recent suggestion of Bechert et al. (1990) and of Luchini et al. (1991), who linked riblet effectiveness to the difference between the protrusion heights for the longitudinal flows and the cross-flows. When the actual geometries are considered, a linear correlation is found between $\Delta h_p/s$ and the maximum amount of drag reduction ΔD_{max}.

Finally, a simple method for the prediction of the drag reduction produced by ribletted surfaces is derived, based on the analysis of the above-mentioned mechanisms. Drag predictions are in close agreement with a large number of well-documented experimental data. This result not only is interesting in itself, but also can be interpreted as an a posteriori confirmation of the validity of the mechanisms proposed for the interaction of the riblets with the turbulent boundary layer.

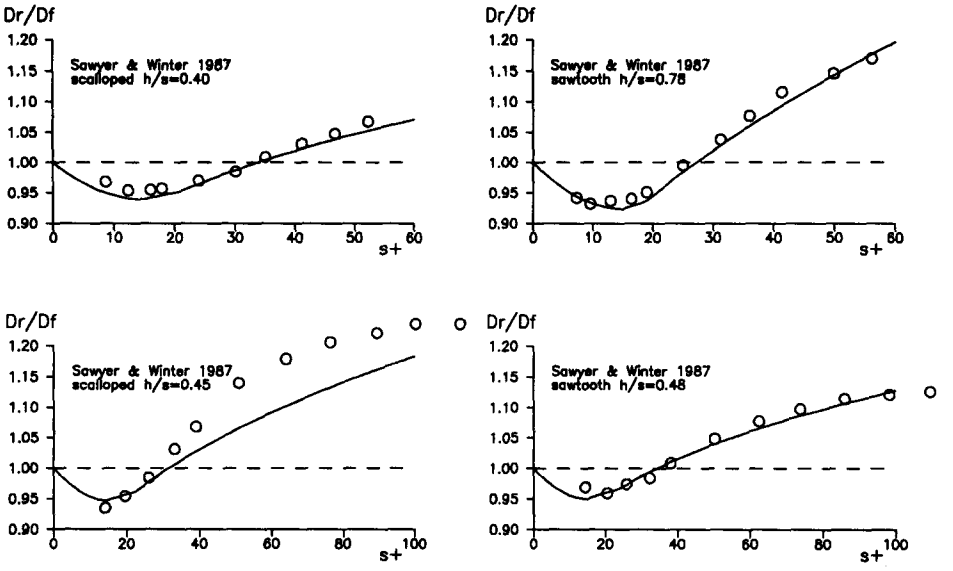

Figure 9 Comparison between measured (symbols) and predicted (solid lines) drag data for various ribletted surfaces. Experimental data from Sawyer and Winter (1987)

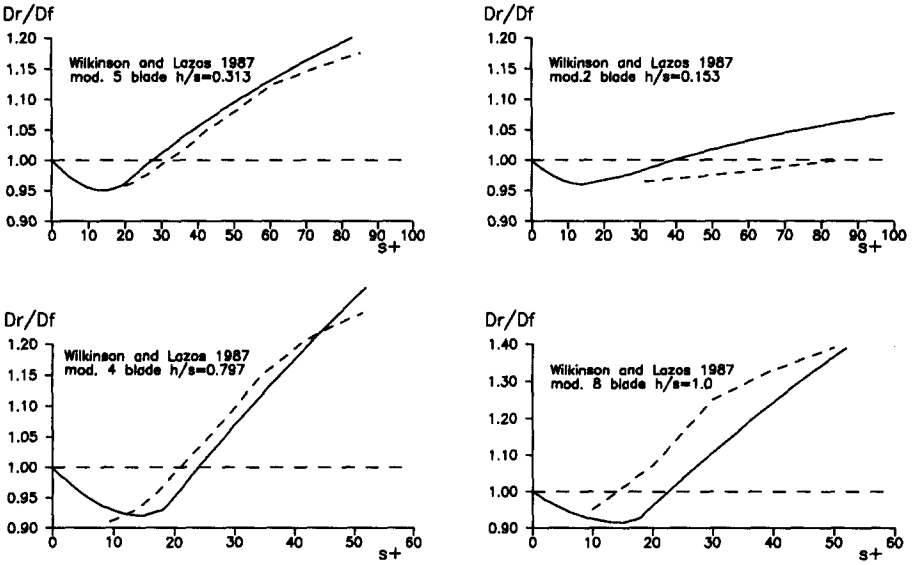

Figure 10 Comparison between measured (dotted lines) and predicted (solid lines) drag data for various ribletted surfaces. Experimental data from Wilkinson and Lazos (1987)

Acknowledgments

This work has been supported, during 1987 and 1989, by the Ministero dell'Università e della Ricerca Scientifica e Tecnologica. The second author wishes to express his gratitude to Professors Franco Camanni and Franca Pellò for their invaluable help during the execution of the present study.

References

Bacher, E. V. and Smith, C. R. 1985. A combined visualization-anemometry study of the turbulent drag reducing mechanism of triangular micro-groove surface modifications. AIAA Paper 85-0548.

Baron, A., Quadrio, M., and Vigevano, L. 1989. Riduzione della resistenza di attrito in correnti turbolente e altezza di protrusione di pareti scanalate. *L'Aerotecnica Missili e Spazio*, **68**, 129

Bechert, D. W., Hoppe, G., and Reif, W. -E. 1985. On the drag reduction of the shark skin. AIAA Paper 85-0546

Bechert, D. W., Bartenwerfer, M., Hoppe, G., and Reif, W.-E. 1986. Drag reduction mechanisms derived from shark skin. AIAA Publ. ICAS-86-1.8.3, 1044

Bechert, D. W., and Bartenwerfer, M. 1987. Die viskose Strömung über Oberflächen mit Längsrippen. DFVLR-FB 97-21 (in German)

Bechert, D. W., and Bartenwerfer, M. 1989. The viscous flow on surfaces with longitudinal ribs. *J. Fluid Mechanics*, **206**, 105–129

Bechert, D. W., Bartenwerfer, M., and Hoppe, G. 1990. Turbulent drag reduction by nonplanar surfaces—A survey on the research at TU/DLR Berlin. In *Structure of Turbulence and Drag Reduction*, A. Gyr (ed.). Springer-Verlag, Berlin

Blackwelder, R. F., and Eckelmann, H. 1979. Streamwise vortices associated with the bursting phenomenon. *J. Fluid Mechanics*, **94** (3), 577–594

Choi, K.-S. 1989. Near-wall structure of a turbulent boundary layer with riblets. *J. Fluid Mechanics*, **208**, 417–458

Choi, K.-S., Pearcey, H. H., and Savill, A. M. 1987. Test of drag reducing riblets on a one-third scale racing yacht. *Proc. Int. Conf. Royal Aeronautical Society on Turbulent Drag Reduction by Passive Means*, London

Coustols, E., Cousteix, J., and Belanger, J. 1987. Drag reduction performance of riblet surfaces and through outer layer manipulators. *Proc. Int. Conf. Royal Aeronautical Society on Turbulent Drag Reduction by Passive Means*, London

Davies, R. T. 1979. Numerical methods for coordinate generation based on Schwarz–Christoffel transformations. AIAA Paper 79–1463

Djenidi, L., Squire, L. C., and Savill, A. M. 1991. High resolution conformal mesh computations for V, U or L groove riblets in laminar and turbulent boundary layers. In *Recent Developments in Turbulence Management*, K. S. Choi (ed.). Kluwer Academic Publishers, Boston, 65–92

Floryan, J. M. 1986. Conformal-mapping-based coordinate generation method for flows in periodic configurations. *J. Comput. Phys.*, **62**, 221–247

Gallagher, J., and Thomas, A. S. W. 1984. Turbulent boundary layer characteristics over streamwise grooves. AIAA Paper 84-2185

Gueznnec, Y. G., Piomelli, U., and Kim, J. 1989. On the shape and dynamics of wall structures in turbulent channel flow. *Phys. Fluids A*, **1**, 764

Johansson, A. V., Alfredsson, P. H., and Kim, J. 1991. Evolution and dynamics of shear-layer structures in near-wall turbulence. *J. Fluid Mechanics*, **224**, 579–599

Kline, S. J., Reynolds, W. C., Schraub, F. A., and Runstadler, P. W. 1967. The structure of turbulent boundary layers. *J. Fluid Mechanics*, **30**, 741

Landahl, M. T. 1990. On sub-layer streaks. *J. Fluid Mechanics*, **212**, 593

Luchini, P., Manzo, F., and Pozzi, A. 1991. Resistance of a grooved surface to parallel flow and cross-flow. *J. Fluid Mechanics*, **228**, 87–109

McLean, D. J., George-Falvy, D. N., and Sullivan, P. P. 1987. Flight-test of turbulent skin-friction reduction by riblets. *Proc. Int. Conf. Royal Aeronautical Society on Turbulent Drag Reduction by Passive Means*, London

Sawyer, W. G., and Winter, K. G. 1987. An investigation of the effect on turbulent skin friction of surfaces with streamwise grooves. *Proc. Int. Conf. Royal Aeronautical Society on Turbulent Drag Reduction by Passive Means*, London

Squire, L. C., and Savill, A. M. 1987. Some experiences of riblets at transonic speeds. *Proc. Int. Conf. Royal Aeronautical Society on Turbulent Drag Reduction by Passive Means*, London

Walsh, M. J. 1982. Turbulent boundary layer drag reduction using riblets. AIAA Paper 82-0169

Walsh, M. J. 1990a. Riblets. *Prog. Astronaut. Aeronaut.*, **123**, 203–261

Walsh, M. J. 1990b. Effect of detailed surface geometry on riblet drag reduction performance. *J. Aircraft*, **27** (6), 572–573

Walsh, M. J., and Weinstein, L. M. 1978. Drag and heat transfer on surfaces with small longitudinal fins. AIAA Paper 78-1161

Walsh, M. J., and Lindemann, A. M. 1984. Optimization and application of riblets for turbulent drag reduction. AIAA Paper 84-0347

Wilkinson, S. P., and Lazos, B. S. 1987. Direct drag and hot-wire measurements on thin-element riblet arrays. *IUTAM Symp. Turbulence Management and Relaminarization*, Bangalore, India

Wilkinson, S. P., Anders, J. B., Lazos, B. S., and Bushnell, D. M. 1987. Turbulent drag research at NASA Langley—Progress and planes. *Proc. Int. Conf. Royal Aeronautical Society on Turbulent Drag Reduction by Passive Means*, London